


Nonreciprocal Sound Propagation via Cascaded Time-Modulated Slab Resonators

Sheng Wan¹, Liyun Cao, Yifan Zhu, Mourad Oudich^{1,*}, and Badreddine Assouar^{1,†}
Université de Lorraine, CNRS, Institut Jean Lamour, 54000 Nancy, France

 (Received 4 May 2021; revised 12 October 2021; accepted 7 December 2021; published 27 December 2021)

In this work, we demonstrate nonreciprocal acoustic wave transmission in two-cascaded Fabry-Perot-like slab resonators undergoing time modulation of their effective density. A phase difference is introduced into the time modulation between the two coupled resonators to produce spatial bias to access unidirectional wave propagation. A theoretical model based on plane-wave expansion and the transfer-matrix method is developed to study the Fabry-Perot-based system. The theoretical model allows rapid and precise characterization of the acoustic dispersion, with results in excellent agreement with finite-element-based numerical simulations. We demonstrate acoustic nonreciprocity behavior for the fundamental acoustic mode and further show that, with proper optimization, the coupled Fabry-Perot-based device can achieve nonreciprocal acoustic frequency conversion. This work could inspire the design of simple and compact nonreciprocal acoustic devices for efficient wave control.

DOI: [10.1103/PhysRevApplied.16.064061](https://doi.org/10.1103/PhysRevApplied.16.064061)

I. INTRODUCTION

During the last decade, a growing area of research is concerned with the possibility of breaking the reciprocity for waves to realize unidirectional wave propagation. Particularly, an acoustic nonreciprocal device, which enables one-way transmission of sound, is highly desirable for numerous technological applications, such as a unidirectional sound barrier, improved medical ultrasound devices, and surface-acoustic-wave-based communication systems [1,2]. Reciprocity is a fundamental property of wave phenomena in any linear time-invariant system [3,4]. It can only be broken using proper biasing of space or time quantities, which are meticulously introduced into the propagation medium. Various systems are constructed to achieve acoustic nonreciprocity and demonstrate different wave behaviors in opposite propagation directions. Early attempts for an acoustic nonreciprocity realization were successfully conducted by combining a nonlinear medium with a phononic crystal [5,6]. Later, geometrical design strategies were proposed to achieve asymmetric wave dispersion, although these systems do not break reciprocity but rather affect the waves packets path [7,8]. The *PT* symmetry can also lead to asymmetric wave reflection by introducing loss and gain elements in a linear waveguide [9].

An exotic way of achieving nonreciprocity is the application of space-time-modulated (STM) mediums to break the time-reversal symmetry. The idea was proposed in

1959 in photonics and electrical circuits, where permittivity, permeability, or impedance is harmonically modulated both in space and time to create unidirectional band gaps for waves [10–12]. The medium can be seen as keeping its intrinsic properties spatially modulated and moving at a certain velocity. This thus breaks the time reversal, allowing different dispersions of waves traveling in opposite directions along the same path. This route, however, faded until this last decade when researchers reinvigorated their interest in the realization of such space-time-modulated systems, all thanks to technological progress in their fabrication and characterization [13–19]. Drawing inspiration from photonics, multiple STM-based designs were proposed in acoustics [20–23] and elastodynamics [24–29]. In those designs, the mechanical properties of the designed mediums were varied in both space and time to achieve nonreciprocity. Additionally, an acoustic circulator [30] is proposed as a nonreciprocal device, which contains circulating flow inside three ports to break time reversal.

However, in most of the works applied to classical waves, and especially in acoustics, the physics of nonreciprocity is based on shifting the Bragg band gap in the frequency domain for opposite directions to prohibit wave-propagation unidirectionally [24–26]. This mechanism is achieved by spatiotemporally modulating the effective parameters of the constituent materials (stiffness) along several periods of the structure (at least 10 periods). Consequently, the periodic parts of the system have to be precisely synchronized, which makes the experimental realization quite challenging, and thus, limit the device's practicability. For instance, in acoustics, although dynamically changing the effective density of air is locally

*mourad.oudich@univ-lorraine.fr

†badreddine.assouar@univ-lorraine.fr

possible [31], a precise harmonic modulation in both space and time along several periods remains challenging. In contrast, nonreciprocity based on STM becomes relatively accessible in elastodynamics by modulating the effective stiffness of the material [26–28]. However, this process involves introducing piezoelectric elements connected to electrical circuits to introduce effective negative capacitance with the complexity of synchronizing the modulations. The whole nonreciprocal device becomes cumbersome, limiting practical applications in the future. Additionally, systems such as coupled modulated Helmholtz resonators [32], air cavities [21], membranes [22], and even Fabry-Perot-based photonic slabs [33] inspire us to find a simpler design than those of the aforementioned systems. For instance, Shen *et al.* [32] show that, using two-cascaded time-modulated Helmholtz resonators (HRs), nonreciprocal wave behavior can be realized via frequency conversion with high-order modes appearing differently for positive and negative propagation. However, nonreciprocity is achieved far from the resonance frequency of the HR as the wave is completely reflected at this frequency. Under this restriction, the fundamental mode with the frequency of the incident wave is always accompanied with high-order modes in the transmission regardless of the direction of propagation. Nevertheless, the choice of cascaded slabs is more advantageous, since it allows high wave transmission at the Fabry-Perot resonance. Consequently, the slab-based-system has the potential to create the situation of unidirectional wave conversion, for instance, hence offering more control over nonreciprocity via mode conversion.

Here, we demonstrate nonreciprocal acoustic transmission in a finite system based on coupled Fabry-Perot resonators with time modulation of their effective properties. A good nonreciprocity is achieved in our system with a quasi-lossless transmission in one direction and a nearly zero transmission of the fundamental mode in the opposite direction. In contrast to previous works that used the Bragg band gap combined with modulating the effective parameters of the materials along several periods of the structure, our system is composed of two coupled fluid

slabs that behave as coupled Fabry-Perot (FP) resonators, whose density of which, however, is temporally modulated. A spatial bias is introduced to realize nonreciprocal wave propagation by forcing a phase difference on the time-modulated density between the two slabs. This kind of modulation can be easily achieved by periodically compressing the fluid, for instance [31,34]. In such a design, the physical mechanism is mainly based on frequency conversion, where the acoustic energy is transferred from the fundamental mode into higher-order ones [35,36].

The plane-wave-expansion (PWE) method [37] is first adopted to construct the scattering matrix describing the system, which analytically solves the acoustic transmission. The analytical result matches well with the finite-element-method (FEM) simulation results. Then, we take advantage of this model to seek for parameters and configurations that yield good nonreciprocity. Furthermore, under the premise of high nonreciprocity, we also discuss the possibility of unidirectional frequency conversion. The latter is an important wave phenomenon that enables waves to be generated at desired frequencies from an incident wave at different frequencies. Recently, the application of frequency conversion was expanded to the acoustic domain, such as directional loudspeakers and nondestructive evaluation [38,39].

II. DESIGN AND THEORY

We first consider an adiabatic single-slab resonator, as shown in Fig. 1. The background medium is air, the density of which is ρ_0 and sound speed is c_0 , with bulk modulus $\kappa_0 = \rho_0 c_0^2$. The thickness of the slab resonator is d . The medium of the slab resonator is a fluid with a static density higher than that of air. In this model, we assume that the density of the slab can be modulated in time: $\rho_1 = \delta\rho_0[1 + 2M \cos(\Omega t + \phi)]$. As we consider the bulk modulus to be fixed throughout this study ($\kappa_0 = 141.2$ kPa), the speed of sound in the slab resonator is consequently modulated as $c_1 = \sqrt{\kappa_0/\rho_1}$, which yields $c_1 =$

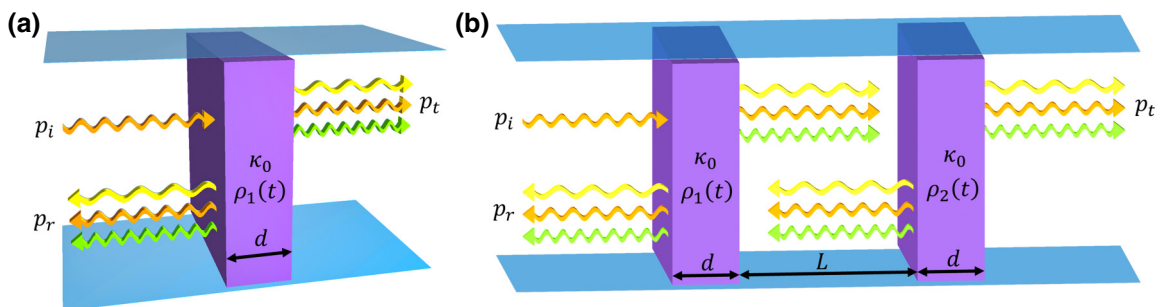


FIG. 1. Schematic of a single-slab (a) system and a two-cascaded-slab (b) system with time-modulated effective densities. Harmonics appear in the transmitted and reflected waves due to modulation.

$\sqrt{\kappa_0/\{\delta\rho_0[1+2M\cos(\Omega t+\phi)]\}}$. Without temporal modulation, the static speed of sound in the slab resonator is $c_1^\delta = c_0/\sqrt{\delta}$.

In practice, this kind of modulation can, for instance, be achieved by driving a piston with rotating elements to induce changing compression in time. Here, δ is the static density ratio, M is the modulation depth, Ω is the angular frequency of modulation, and ϕ is the initial phase of the modulation. Considering a forward incident wave at angular frequency ω , and using the Floquet-Bloch theorem, the acoustic pressure and particle-velocity fields in the slab yield

$$p(x, t) = \sum_{n=-\infty}^{+\infty} p_n(x) e^{j(\omega+n\Omega)t}, \quad (1)$$

$$v(x, t) = \sum_{n=-\infty}^{+\infty} v_n(x) e^{j(\omega+n\Omega)t}, \quad (2)$$

where $p_n(x)$ and $v_n(x)$ are the Fourier components of pressure and velocity, respectively, in the time domain for both forward and backward propagating waves. The time-modulated density can be rewritten in the same way:

$$\rho_1(t) = \delta\rho_0 \sum_{m=-\infty}^{+\infty} \tilde{\rho}_m e^{jm\Omega t} e^{j\phi_m}. \quad (3)$$

According to the adopted harmonic modulation for ρ_1 , we have here $\tilde{\rho}_0 = 1$, $\tilde{\rho}_{\pm 1} = M$, and $\tilde{\rho}_m = 0$ for $m \neq 0, \pm 1$ and $\phi_{\pm 1} = \pm\phi$. By substituting Eqs. (2) and (3) into the known acoustic equation, $\partial_x p = -\rho(t)\partial_t v$, we get

$$\begin{aligned} \frac{\partial p(x, t)}{\partial x} &= -\delta\rho_0 \sum_{m=-\infty}^{+\infty} \tilde{\rho}_m e^{jm\Omega t} e^{j\phi_m} \\ &\times \sum_{n'=-\infty}^{+\infty} j(\omega+n'\Omega) v_{n'}(x) e^{j(\omega+n'\Omega)t}. \end{aligned} \quad (4)$$

Then we develop Eq. (4) by combining the two summations:

$$\begin{aligned} \frac{\partial p(x, t)}{\partial x} &= -j\delta\rho_0 \sum_{n', m} (\omega+n'\Omega) \tilde{\rho}_m v_{n'}(x) \\ &\times e^{j[\omega+(n'+m)\Omega]t} e^{j\phi_m}. \end{aligned} \quad (5)$$

By eliminating the index script m by replacing it with $n - n'$, we can develop Eq. (5) into

$$\begin{aligned} \frac{\partial p(x, t)}{\partial x} &= -j\delta\rho_0 \sum_{n', n} (\omega+n'\Omega) \tilde{\rho}_{n-n'} v_{n'}(x) \\ &\times e^{j\phi_{n-n'}} e^{j(\omega+n\Omega)t}. \end{aligned} \quad (6)$$

By substituting Eq. (1) into Eq. (6) and using the orthogonality of $(e^{jn\Omega t})_n$, we have

$$\frac{\partial p_n(x)}{\partial x} = -j\delta\rho_0 \sum_{n'} (\omega+n'\Omega) \tilde{\rho}_{n-n'} e^{j\phi_{n-n'}} v_{n'}(x). \quad (7)$$

The time-dependent term $e^{j\omega t}$ is eliminated.

Substituting Eqs. (1)–(3) into the known acoustic equation, $\partial_x v = -\kappa_0^{-1} \partial_t p$, and following the same steps as above, we get

$$\frac{\partial v_n(x)}{\partial x} = -j(\omega+n\Omega) \frac{1}{\kappa_0} p_n(x). \quad (8)$$

After further developments by defining a new variable, $\xi = x\Omega/c_1^\delta$, Eqs. (7) and (8) become

$$\frac{\partial p_n(\xi)}{\partial \xi} = -jZ_1^\delta \sum_{n'} \left(\frac{\omega}{\Omega} + n'\right) \tilde{\rho}_{n-n'} e^{j\phi_{n-n'}} v_{n'}(\xi), \quad (9)$$

and

$$\frac{\partial v_n(\xi)}{\partial \xi} = -j \frac{1}{Z_1^\delta} \left(\frac{\omega}{\Omega} + n\right) p_n(\xi), \quad (10)$$

where $Z_1^\delta = \delta\rho_0 c_1^\delta$ is the static impedance in the slab.

Thus, a series of first-order partial differential equations is constructed based on Eqs. (9) and (10), which depends on the number of decompositions, N , we adopt to approximate the solution:

$$\mathbf{A}_s \cdot \begin{pmatrix} \mathbf{p}^N \\ \mathbf{v}^N \end{pmatrix}_s - \mathbf{I} \cdot \partial_\xi \begin{pmatrix} \mathbf{p}^N \\ \mathbf{v}^N \end{pmatrix}_s = \mathbf{0}, \quad (11)$$

where $\mathbf{p}^N = \langle p_{-N}, \dots, p_0, \dots, p_N \rangle^T$, $\mathbf{v}^N = \langle v_{-N}, \dots, v_0, \dots, v_N \rangle^T$, $\mathbf{A}_s = \begin{bmatrix} \mathbf{0} & \mathbf{A}_s^p \\ \mathbf{A}_s^v & \mathbf{0} \end{bmatrix}$, \mathbf{I} is the identity matrix, and subscript s indicates the domain index. For example, in Fig. 2, $s = 1$ refers to the slab resonator, and $s = 2$ refers to the next contact with air medium. \mathbf{A}_s^p and \mathbf{A}_s^v are both square matrices with size $2N + 1$:

$$\mathbf{A}_{s,(n,n')}^p = -jZ_1^\delta \left(\frac{\omega}{\Omega} + n'\right) \tilde{\rho}_{n-n'} e^{j\phi_{n-n'}}, \quad (12)$$

$$\mathbf{A}_{s,(n,n')}^v = -j \frac{1}{Z_1^\delta} \left(\frac{\omega}{\Omega} + n\right) \delta_{n-n'}, \quad (13)$$

where $\delta_{n-n'}$ is the Kronecker function. As \mathbf{A}_s is function of ξ , Eq. (11) has a solution in the following form:

$$\begin{aligned} \begin{pmatrix} \mathbf{p}^N \\ \mathbf{v}^N \end{pmatrix}_s &= \sum_{i=-N}^{+N} \mathbf{C}_{s,i}^+ \mathbf{V}_{s,i}^+ e^{-\lambda_{s,i}^+ [\xi(x) - \xi_0]} \\ &+ \sum_{i=-N}^{+N} \mathbf{C}_{s,i}^- \mathbf{V}_{s,i}^- e^{-\lambda_{s,i}^- [\xi(x) - \xi_0]}, \end{aligned} \quad (14)$$

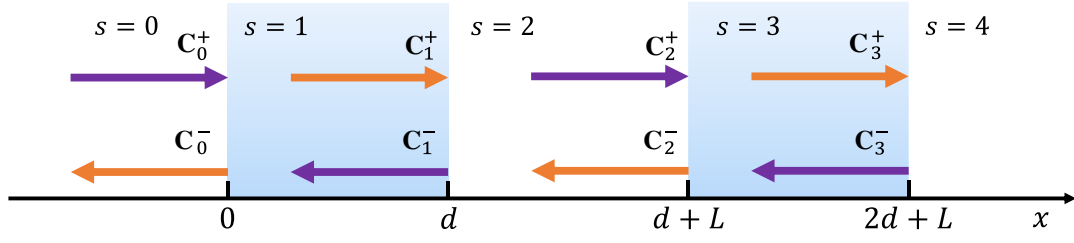


FIG. 2. Schematic of transfer matrix $\mathbf{M}_{s \rightarrow s+1}$ between layers. \mathbf{C}_s^\pm is the complex amplitude of the forward-backward wave at the right boundary of layer s .

where $\mathbf{V}_{s,i}^\pm$ and $\lambda_{s,i}^\pm$ are the i th eigenvector and eigenvalue associated with matrix \mathbf{A}_s , respectively, corresponding to forward or backward wave propagation associated with layer s ; $\mathbf{C}_{s,i}^\pm$ are unknown coefficients, which correspond to wave amplitudes. By considering the boundary conditions (continuity of pressure and velocity) between the layers in contact, labeled s and $s+1$, and performing some algebraic manipulations, we can easily obtain transfer matrix $\mathbf{M}_{s \rightarrow s+1}$, which is defined by

$$\begin{pmatrix} \mathbf{C}_{s+1}^+ \\ \mathbf{C}_{s+1}^- \end{pmatrix} = \mathbf{M}_{s \rightarrow s+1} \begin{pmatrix} \mathbf{C}_s^+ \\ \mathbf{C}_s^- \end{pmatrix}. \quad (15)$$

The definition of \mathbf{C}_s^\pm is explained in Fig. 2. $\mathbf{M}_{s \rightarrow s+1}$ can be developed from Eq. (14) and the boundary conditions:

$$\mathbf{M}_{s \rightarrow s+1} = \langle \mathbf{V}_{s+1}^+ | \mathbf{V}_{s+1}^- \rangle^{-1} \langle \mathbf{V}_s^+ | \mathbf{V}_s^- \rangle \begin{pmatrix} \mathbf{H}_s & \mathbf{0} \\ \mathbf{0} & \mathbf{H}_s^{-1} \end{pmatrix}, \quad (16)$$

where $\mathbf{H}_s = \begin{pmatrix} \mathbf{H}_s^+ & \mathbf{0} \\ \mathbf{0} & \mathbf{H}_s^- \end{pmatrix}$, $\mathbf{H}_{s,(n,n')}^\pm = e^{-\lambda_{s,n-N-1}^\pm (l_s \Omega / c_s)} \delta_{n-n'}$, and $\mathbf{V}_s^\pm = \langle V_{s,-N}^\pm, \dots, V_{s,0}^\pm, \dots, V_{s,N}^\pm \rangle$. l_s is the thickness of layer s ; c_s is the speed of sound in layer s .

From Eq. (15), we construct transfer matrix \mathbf{M} to describe the complete system presented in Fig. 2:

$$\mathbf{M} = \prod_i^X \mathbf{M}_{(X-i) \rightarrow (X+1-i)}. \quad (17)$$

The above solution is based on the PWE and the precision of the solution is related to the considered number, N , of plane waves. In our work, the convergence of the result is guaranteed with $N \geq 4$. Finally, we obtain the scattering matrix, \mathbf{S} , from the transfer matrix, \mathbf{M} (see Appendix A).

Using the vector describing the incident wave of positive direction $\mathbf{J}^+ = \langle \delta_N, \dots, \delta_0, \dots, \delta_{-N} | \mathbf{0}^N \rangle^T$, we can deduce the corresponding reflection and transmission coefficients; δ_n is Kronecker function:

$$\begin{pmatrix} \mathbf{r}^{N,+} \\ \mathbf{t}^{N,+} \end{pmatrix} = \mathbf{S} \cdot \mathbf{J}^+, \quad (18)$$

where $\mathbf{r}^{N,+} = \langle r_N^+, \dots, r_0^+, \dots, r_{-N}^+ \rangle^T$ and $\mathbf{t}^{N,+} = \langle t_N^+, \dots, t_0^+, \dots, t_{-N}^+ \rangle^T$. Similarly, the reflection and transmission coefficients for negative incidence can be obtained using the vector associated with the negative incident wave, $\mathbf{J}^- = \langle \mathbf{0}^N | \delta_{-N}, \dots, \delta_0, \dots, \delta_N \rangle^T$:

$$\begin{pmatrix} \mathbf{t}^{N,-} \\ \mathbf{r}^{N,-} \end{pmatrix} = \mathbf{S} \cdot \mathbf{J}^-, \quad (19)$$

where $\mathbf{t}^{N,-} = \langle t_N^-, \dots, t_0^-, \dots, t_{-N}^- \rangle^T$ and $\mathbf{r}^{N,-} = \langle r_N^-, \dots, r_0^-, \dots, r_{-N}^- \rangle^T$ are the corresponding transmission and reflection coefficients, respectively.

These equations allow us to evaluate the transmission and reflection coefficients for each frequency order. We perform a series of calculations using our theoretical model to determine the optimized design that enables unidirectional propagation and frequency conversion. The parameters involved for our optimization process are the incident angular frequency, ω ; the modulation frequency, Ω ; the static density ratio, δ ; and the phase difference between the modulations of the slabs, $\Delta\phi = \phi_1 - \phi_2$.

III. RESULTS AND DISCUSSION

A. Single-slab resonator

In the present study, the considered intrinsic parameters for air at ambient temperature are $\rho_0 = 1.2 \text{ kg/m}^3$ and $c_0 = 343 \text{ m/s}$. Since the acoustic equations are linear in this study, we consider normalized incident frequency $F_{\text{in}} = \omega / (2\pi f_r^\delta)$ and normalized modulation frequency $F_m = \Omega / (2\pi f_r^\delta)$, where $f_r^\delta = c_1^\delta / (2d)$ is the resonance frequency of the slab without temporal modulation.

Figure 3 shows the transmission results for the case of $\delta = 5$, $F_m = 1.12$, and $N = 5$. In such a configuration, since the modulation rate is relatively low, the conversion from the fundamental mode to higher-order harmonics ($|n| \geq 3$) can be omitted, so only $n = 0, \pm 1, \pm 2$ are shown in the figure. Figure 3(a) displays the transmission curves for the static case without modulation (black curve) and the transmission coefficients for the temporally modulated slab for orders $i = 0, \pm 1, \pm 2$, as a function of the incident frequency. We can see that, under temporal modulation,

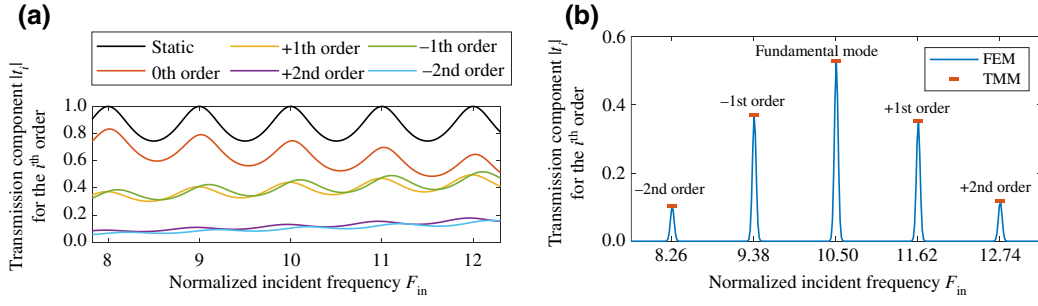


FIG. 3. Transmission through a single time-modulated slab. (a) Calculated transmission in the static case (black solid line) and transmission components, $|t_i|$, for i th order up to second order. Modulation frequency in this case is $F_m = 1.12$. (b) Transmission spectrum for an incident monochromatic wave at frequency $F_{in} = 10.5$. Blue solid curve stands for the spectrum obtained from the time-dependent FEM simulation, while red blocks stand for theoretically predicted transmission coefficients for the zeroth, \pm first, and \pm second orders (TMM).

part of the energy of the fundamental mode is converted to higher orders modes located at $F_{in} \pm nF_m$. It indicates that if the system is properly tuned, the frequency conversion could be stronger, then the nonreciprocity is possible with some spatial bias involved. Further, we confronted these results with numerical ones from simulations based on the FEM via the commercial software COMSOL Multiphysics v5.5. A comparison is shown in Fig. 3(b) for the chosen case of the monochromatic incident wave with frequency $F_{in} = 10.5$. Because of the existence of time-varying parameters, the FE simulations are performed in the time domain. The length of the input signal has to be much longer than the modulation period, $T_m = 2\pi/\Omega$, to guarantee the stability and accuracy of the result. In Fig. 3(b), the response of the time-modulated slab is analyzed via Fourier transform. Good agreement between theory (flat symbols) and simulation (blue solid lines) is observed.

B. Bilayer-slab resonator

As shown in Fig. 1(b), spatial bias is introduced into the system by adding a second time-modulated slab resonator with a different initial phase. We consider two slabs with the same thickness, d , located at $x = 0$ and $x = L + d$, with air medium of length L between them. The inner air medium can be seen as a resonator as well, the resonance frequency of which is $f_g = c_0/2L$. To achieve good nonreciprocity with this system, we tune the incident frequency, F_{in} ; the modulation frequency, Ω ; the static density ratio, δ ; and the phase difference, $\Delta\phi$, between the modulations of the two slabs, within certain ranges. Our strategy to achieve nonreciprocity is based on two-level tuning. First, we tune F_{in} and F_m with properly preselected $\Delta\phi$ and δ . By analyzing the diagrams of transmittance asymmetry difference, $|T_0^+ - T_0^-|$ (with $T_0^+ = |t_0^+|^2$ and $T_0^- = |t_0^-|^2$); their ratio, $|10 \log_{10}(T_0^+/T_0^-)|$; and the total transmission difference, $\left| \left(\sum_{-N}^N T_i^+ \right)^{1/2} - \left(\sum_{-N}^N T_i^- \right)^{1/2} \right|$, we were able to select a

proper set of F_{in} and F_m . Afterwards, a fine optimization is performed by tuning $\Delta\phi$ and δ with fixed F_{in} and F_m . To acquire nonreciprocity at a specific frequency, we can scale the slab dimension, d , with the tuned parameters.

The coupling behavior of the resonators in the static state (without modulation) has a significant effect on nonreciprocity. Definite static coupling behavior reduces variable elements in the tuning process. To characterize the coupling behavior, we introduce a coupling factor, $\alpha = f_g/f_r^\delta$; the ratio between the resonance frequency of the inner air waveguide, $f_g = c_0/2L$; and the static slab resonance frequency, f_r^δ . In what follows, we use the configuration of $\alpha = 1$ (see Appendix B).

The static density ratio, δ , determines the effective sound speed and the effective density in the slab medium, and thus, its static impedance. Therefore, it affects directly the scattering behavior on the boundary between slab and air, because this density change leads to mismatched impedance on the boundary, which impacts on the wave reflection and transmission. As δ is larger, this scattering becomes stronger, which contributes to wave asymmetry under spatial bias. However, large δ weakens the feasibility of the system. To be more realistic, we set $\delta = 5$. The thickness of the slab is set as $d = 0.05$ m, and the length of the air medium, L , is determined by $L = \sqrt{\delta}d/\alpha$.

The density of the two-cascaded slabs is time modulated as $\rho_1 = \delta\rho_0[1 + 2M \cos(\Omega t)]$ and $\rho_2 = \delta\rho_0[1 + 2M \cos(\Omega t + \Delta\phi)]$, where the phase difference, $\Delta\phi$, is taken into account. In what follows, we utilize 0.5π as the preset value of $\Delta\phi$, which leads to spatiotemporal bias and breaks the time-reversal symmetry. When $\Delta\phi = 0$, the system complies with time-reversal symmetry, as the bilayer-slab resonator system is symmetric. When $\Delta\phi = \pi$, although time-reversal symmetry is broken, it leads only to phase inversion between the wave transmitted in opposite directions, while the amplitudes are kept the same. As asymmetry appears in $\Delta\phi \in (0, \pi)$, while we get no asymmetry at both limits of this range, an extremum

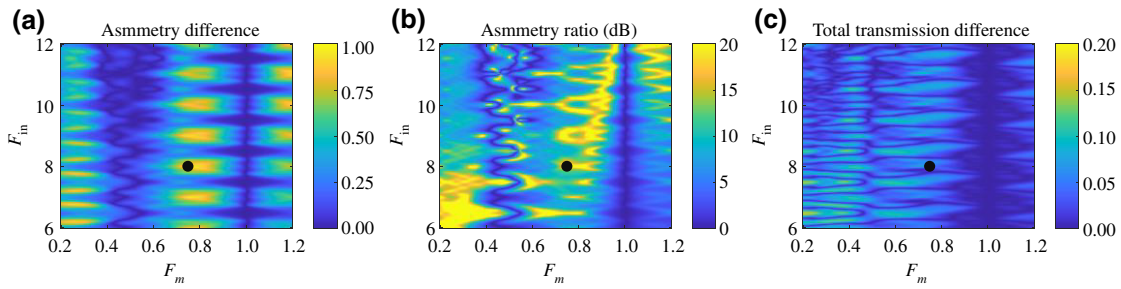


FIG. 4. Transmission analysis between right and left propagations as function of the normalized incident frequency F_{in} and the normalized modulation frequency F_m , for $\Delta\phi = 0.5\pi$ and $\delta = 5$. (a) Asymmetry difference of the zeroth-order-mode transmittance, representing $|T_0^+ - T_0^-|$. (b) Asymmetry ratio of zeroth-order-mode transmittance, representing $|10\log_{10}(T_0^+/T_0^-)|$. (c) Total transmission difference, representing $\left| \left(\sum_{-N}^N T_i^+ \right)^{1/2} - \left(\sum_{-N}^N T_i^- \right)^{1/2} \right|$, where all the modes are included. Black dots mark the points where $F_{\text{in}} = 8$ and $F_m = 0.76$.

exists. Consequently, we first choose $\Delta\phi = 0.5\pi$, where we expect to have the maximum effect of asymmetry (see Appendix C).

The modulation depth, M , is directly related to the external energy brought into the system actively, so practically we tend to adopt relatively small values for the modulation depth. A weak modulation not enables only the feasibility of the system, but also prevents the transmitted wave from being overamplified by the modulation. Here, the modulation depth is chosen to be $M = 0.06$. Then, we first search for nonreciprocal wave behavior by sweeping the incidence frequency, F_{in} , and the modulation frequency, F_m .

Here, we are interested in the scattering properties of the fundamental mode. Figures 4(a) and 4(b) show the quantities $|T_0^+ - T_0^-|$ and $|10\log_{10}(T_0^+/T_0^-)|$, respectively, for the fundamental mode as a function of the normalized modulation frequency, F_m , and incident frequency, F_{in} . Figure 4(c) plots the normalized total transmission difference for the convenience of observation. The criteria for finding nonreciprocity are $|T_0^+ - T_0^-| > 0.9$ and $|10\log_{10}(T_0^+/T_0^-)| > 20$ dB in a wide range of F_{in} , which correspond to yellow zones that are wide on the F_{in} axis in the plots. As shown in Fig. 4(c), it is difficult to achieve high-level asymmetry of total transmission in this system, so the nonreciprocity here is mainly due to frequency conversion. We observe that Figs. 4(a) and 4(b) show some periodicity on the F_{in} axis. The nonreciprocity zones tend to appear at multiples of the resonance frequency of the slab, for example, the marked point where $F_{\text{in}} = 8$ corresponds to the actual frequency, $8f_r^\delta$. In fact, far away from resonances, the reflection is dominant, and the effect of frequency conversion on the transmitted waves becomes weak. Another interesting phenomenon reflected in Fig. 4 is that, when $F_m = 1$, all asymmetries disappear. In this case, the actual modulation frequency is equal to the resonance frequency of the slab, $f_m = f_r^\delta$. In this case, the

spatial-biasing effect from the phase difference becomes weak.

For an optimized case of nonreciprocity, we select $F_{\text{in}} = 8$ and $F_m = 0.76$, where $|T_0^+ - T_0^-| = 0.956$ and $|10\log_{10}(T_0^+/T_0^-)| = 25.98$ dB (black dots in Fig. 4). In this configuration, the positive and negative transmission coefficients of the fundamental mode are $t_0^+ = 0.049$ and $t_0^- = 0.979$. While fixing the same values of F_{in} and F_m , we perform a second-level fine-tuning, where we sweep for δ and $\Delta\phi$ (see Appendix D). A better result is achieved with $\Delta\phi = 0.46\pi$ and $\delta = 5$.

With this fine optimization, the transmission coefficients become $t_0^+ = 0.043$ and $t_0^- = 0.979$, so nonreciprocal transmission is slightly improved in comparison with the previous result. For this configuration, we plot in Fig. 5 the transmission coefficient in both propagation directions with an incident monochromatic wave at a frequency of $F_{\text{in}} = 8$ [Figs. 5(a) and 5(b)]. We can clearly see that the zeroth-order mode is dominant in the negative propagation direction, while it is almost depleted in the positive direction with strong frequency conversion at higher-order modes. We also plot the fundamental-mode transmission in both propagation directions in Fig. 5(c), where we can deduce acoustic nonreciprocity around the incident frequency. The bandwidth of nonreciprocity is defined as $|T_0^+(\omega) - T_0^-(\omega)| > 0.5 \max(|T_0^+ - T_0^-|)$. The normalized bandwidth of nonreciprocity, ΔF , is approximately 0.51 in this case.

To further illustrate the nonreciprocity behavior, we plot in Fig. 6 the total pressure as a function of space and time based on the transit FEM simulation. The figure shows the total pressure on the whole structure within a chosen duration of time. In the negative direction [Fig. 6(a)], the incident wave can pass through our structure and the wave form is little distorted, indicating transmission of the fundamental mode with relatively low reflection, in contrast to that of the positive direction. However, in

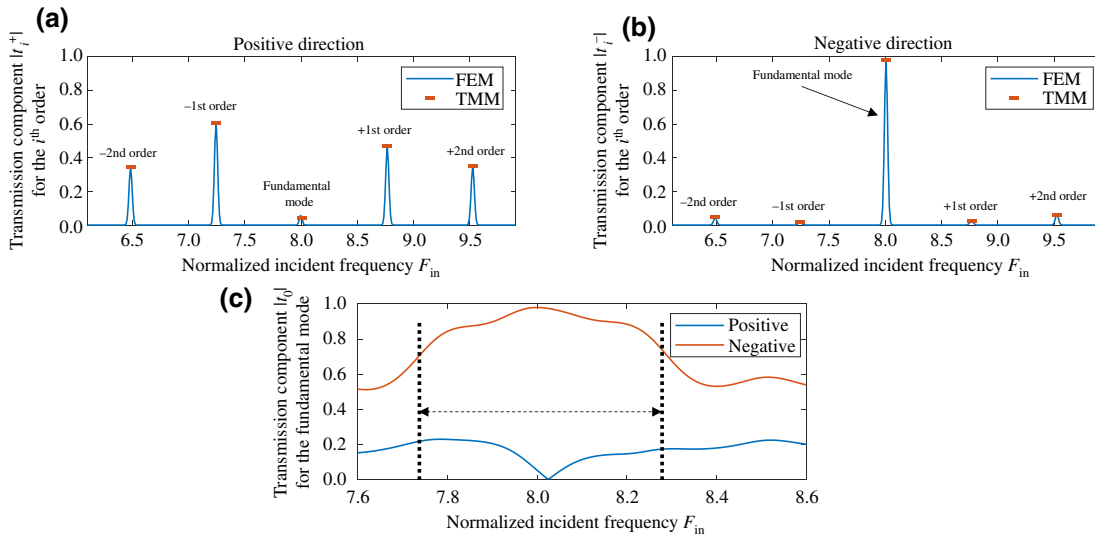


FIG. 5. Transmission coefficients for the positive direction (a) and the negative direction (b) with $F_{in} = 8$, $F_m = 0.76$, $\Delta\phi = 0.46\pi$, and $\delta = 5$. (c) Theoretically calculated transmission coefficient curve for the fundamental mode (zeroth order) for both directions as a function of F_{in} , for $F_m = 0.76$, $\Delta\phi = 0.46\pi$, and $\delta = 5$. Black dashed lines and arrows mark the bandwidth.

the positive direction [Fig. 6(b)], we observe a different wave-propagation phenomenon, where the pattern of the fundamental mode is no longer dominant, and frequency conversion to higher-frequency orders is observed. The modulation-wave behavior shown in Fig. 6(b), which corresponds to the superposition of several harmonic waves (\pm first order, \pm second order, etc.)

C. Unidirectional frequency conversion

Since the nonreciprocity in our system is achieved because of frequency conversion, we further exploit unidirectional frequency conversion under the nonreciprocity premise. As schematically shown in Fig. 7, for a harmonic excitation, if the modulation frequency is chosen

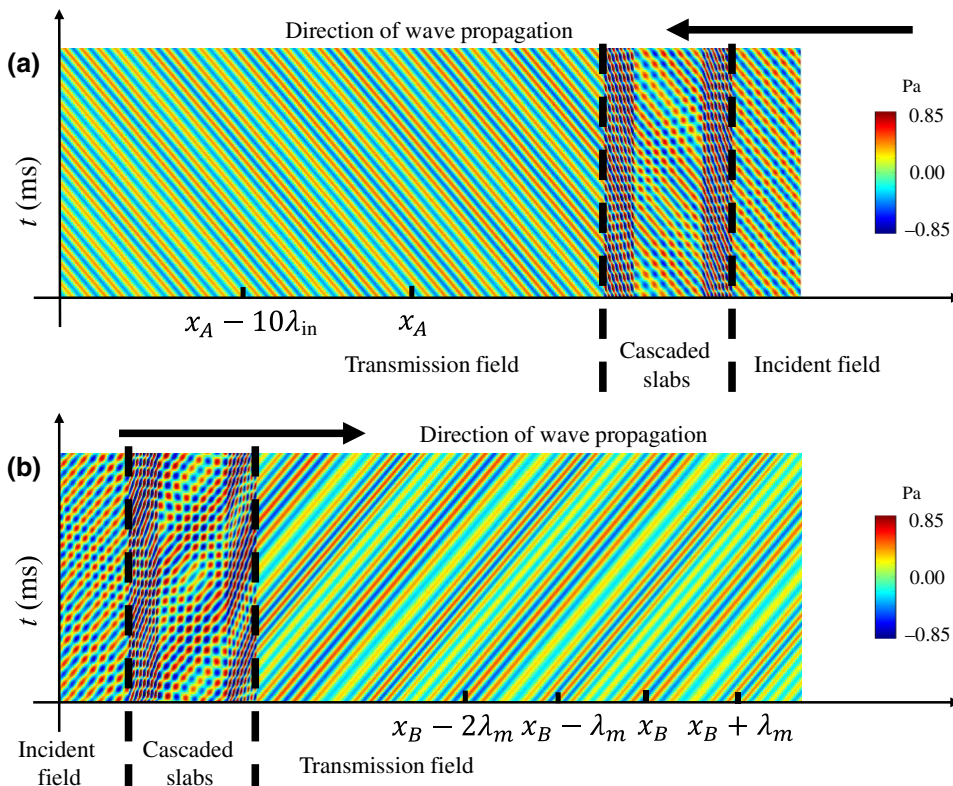


FIG. 6. Pressure-field pattern for the case reported in Figs. 5(a) and 5(b), from 30 to 31 ms. $\lambda_{in} = 1/f_{in}$ is the wavelength of the incident wave and $\lambda_m = 2\pi/\Omega$ is the modulation wavelength: (a) negative direction; (b) positive direction.

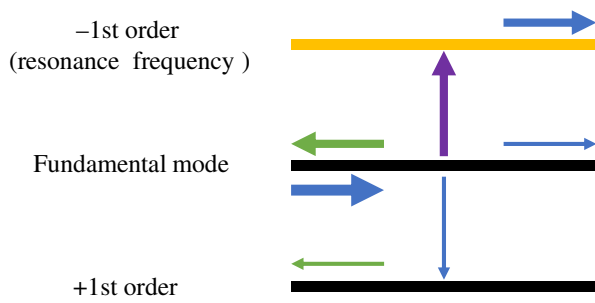


FIG. 7. Schematic of frequency conversion. $-$ First-order mode is at the resonance frequency of the slab instead of the fundamental mode and the $+$ first-order mode. Thus, $-$ first-order mode may be transmitted with higher amplitude.

so that the $-$ first-order corresponds to one of the resonance frequencies of the slab, this $-$ first-order mode can be highly transmitted. There are numerous possibilities for frequency conversion, so we consider, for instance, two of them: from zeroth to $-$ first and from zeroth to $+$ first, which are shown by vertically oriented arrows. In the example of Fig. 7, if we choose a specific frequency of modulation so that the $-$ first order corresponds to one of the resonance frequencies of the slab, this order could be highly transmitted, while the fundamental mode and the $+$ first order are weakly transmitted. Furthermore, if high transmission exists at both the fundamental mode and one of the \pm first-order modes due to large transmission bandwidth, we can achieve both unidirectional frequency conversion and nonreciprocity by manipulating the modulation.

To illustrate this idea, we consider the configuration of $F_m = 0.85$, $\Delta\phi = 0.589\pi$, and $\delta = 12$, where strong asymmetries of all \pm first-order and zeroth-order modes are achieved. We plot in Fig. 8(a) the transmission coefficient in the frequency domain for the zeroth and \pm first orders. We can observe that the \pm first-order modes are both dominant in the transmission for one of the directions of propagation. At $F_{in} = 8.85$, for instance, the $-$ first-order mode ($F_{in} - F_m$) is at a resonance frequency ($8f_r^\delta$). Figures 8(b) and 8(c) display the transmission coefficients with an incident monochromatic wave at $F_{in} = 8.85$. In the positive direction, the amplitude of the $-$ first-order mode reaches 0.61 and becomes the dominant mode, and the amplitude of the fundamental mode is 0.18, while, in the negative direction, the fundamental mode's amplitude is 0.78 and the amplitudes of all neighboring modes are low. In this case, unidirectional frequency conversion appears.

Regarding the experimental implementation of the system, for instance, it can be built using successive layers of air and gas with different densities, separated by an airtight thin membrane to avoid being mixed. Then, the effective density can be modulated in time using pistons that can change the volume of each cavity layer. The thickness of the layers can be chosen to operate at frequency ranges far from the flexural resonances of the membranes. The existence of the membranes will only slightly reduce the bandwidth of nonreciprocity, which can still be achieved by fine-tuning the parameters of the system.

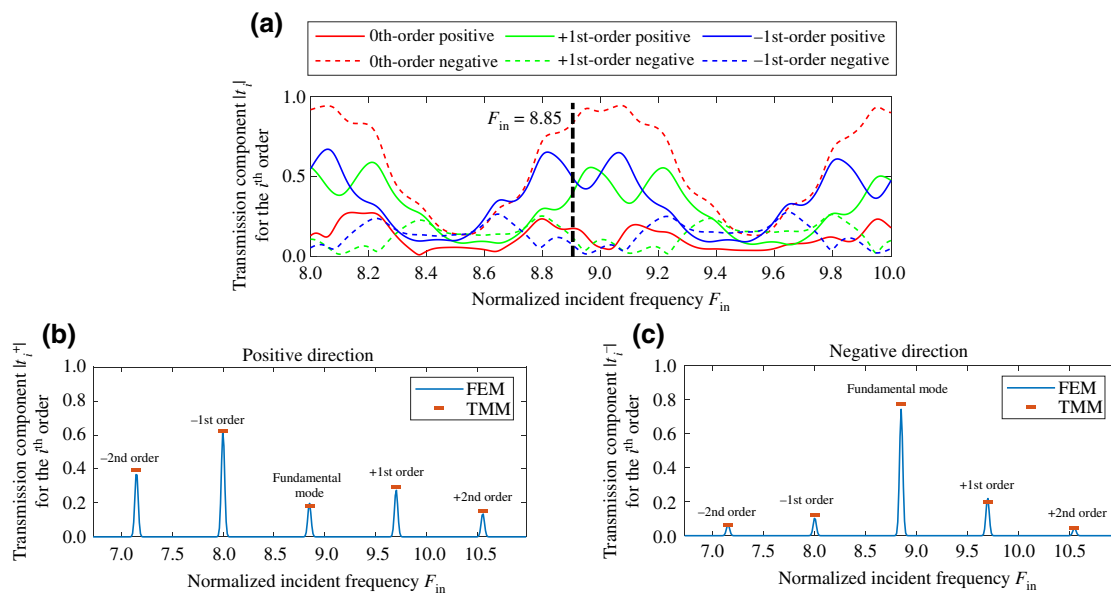


FIG. 8. (a) Transmission coefficient in the frequency domain for the zeroth, \pm first, and \pm second orders with $F_m = 0.85$, $\Delta\phi = 0.589\pi$, and $\delta = 12$. Transmission spectrum coefficient in the positive direction (a) and the negative direction (b) at monochromatic incident frequency $F_{in} = 8.85$ (blocks indicate theoretical results and solid blue line represents FEM-based simulation).

IV. CONCLUSION

Here, we demonstrate nonreciprocal acoustic transmission and unidirectional-frequency conversion in cascaded fluid-slab resonators based on temporal modulation of their effective densities, with a phase difference of the time modulations between the slabs. A theoretical transfer-matrix method based on plane-wave expansion is developed for efficient characterization of the acoustic dispersion of the system, while numerical simulations based on the FEM are conducted to assess the theoretical findings. Optimization of the system's parameters is carried out to achieve broadband nonreciprocity and frequency conversion in the two-slab system. Acoustic nonreciprocity behavior is demonstrated for a monochromatic incident wave, with almost 97.9% transmission in the positive direction, while only 4.3% is transmitted in the negative direction. Furthermore, unidirectional frequency conversion is achieved. Over half of the transmitted acoustic energy is converted into one mode with a higher static density ratio, δ . The proposed design of a nonreciprocal acoustic system displays promising functionalities, with a simple compact configuration to achieve unidirectional wave-propagation and frequency conversion. Although the present system is purely theoretical and far from representing a realistic device for application, it is possible to imagine a solid system where we consider only longitudinal waves, which are described with the same Helmholtz equation, and thus, behaves the same as acoustic waves in a fluid. In this case, our approach can also be conducted by considering time modulation of the effective stiffness of the materials using piezoelectric elements instead of density. Furthermore, the time-modulation capability of the design is to be investigated, especially when the frequency of modulation is comparable to the incident frequency of the system. Our design offers a platform that can inspire future devices for multiple applications, including biomedical ultrasound

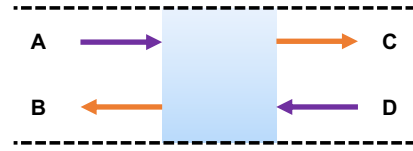


FIG. 9. Schematic of the system for matrix conversion.

devices, improved energy harvesting, and communication systems.

APPENDIX A: CONVERSION FROM TRANSFER MATRIX TO SCATTERING MATRIX

The schematic of the scattering system is shown in Fig. 9. The transfer matrix, \mathbf{M} , and the scattering matrix, \mathbf{S} , are defined as

$$\begin{pmatrix} \mathbf{C}^N \\ \mathbf{D}^N \end{pmatrix} = \begin{pmatrix} \mathbf{M}_{11} & \mathbf{M}_{12} \\ \mathbf{M}_{21} & \mathbf{M}_{22} \end{pmatrix} \begin{pmatrix} \mathbf{A}^N \\ \mathbf{B}^N \end{pmatrix},$$

$$\begin{pmatrix} \mathbf{B}^N \\ \mathbf{C}^N \end{pmatrix} = \begin{pmatrix} \mathbf{S}_{11} & \mathbf{S}_{12} \\ \mathbf{S}_{21} & \mathbf{S}_{22} \end{pmatrix} \begin{pmatrix} \mathbf{A}^N \\ \mathbf{D}^N \end{pmatrix},$$

where $\mathbf{A}^N = \langle A_{-N}, \dots, A_N \rangle^T$, $\mathbf{B}^N = \langle B_{-N}, \dots, B_N \rangle^T$, $\mathbf{C}^N = \langle C_{-N}, \dots, C_N \rangle^T$, and $\mathbf{D}^N = \langle D_{-N}, \dots, D_N \rangle^T$.

\mathbf{M}_{11} , \mathbf{M}_{12} , \mathbf{M}_{21} , and \mathbf{M}_{22} are matrices with $2N + 1$ orders. With some algebraic manipulations, we can easily obtain the elements of the scattering matrix from the

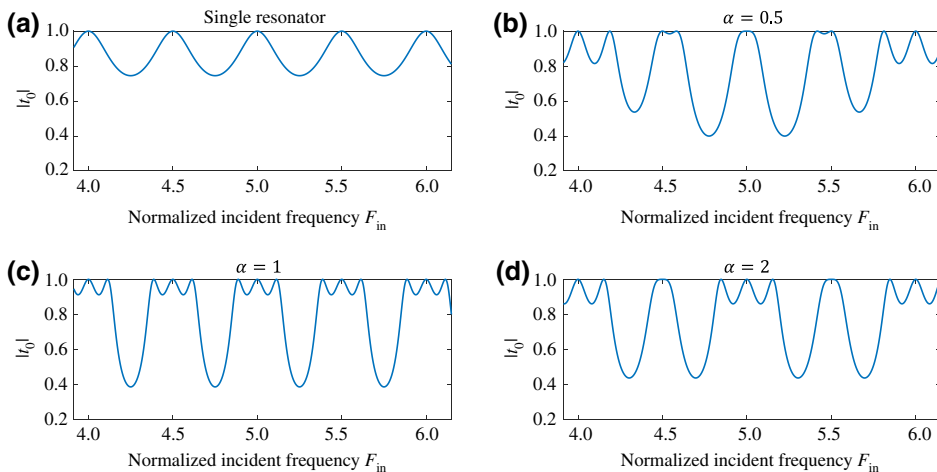


FIG. 10. Transmission coefficients for the static case (without time modulation): (a) single resonator, (b) cascaded resonators with $\alpha = 0.5$, (c) cascaded resonators with $\alpha = 1$, and (d) cascaded resonators with $\alpha = 2$.

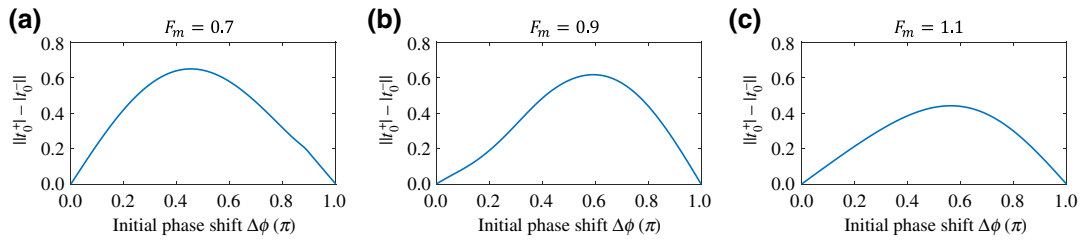


FIG. 11. Transmission coefficient difference, $||t_0^+ - |t_0^-||$, of the fundamental mode as a function of $\Delta\phi$ for an incident wave frequency of $F_{in} = 8.94$, for the case of frequency modulations $F_m = 0.7$ (a), $F_m = 0.9$ (b), and $F_m = 1.1$ (c).

transfer matrix:

$$\mathbf{S}_{11} = -\mathbf{M}_{22}^{-1} \cdot \mathbf{M}_{21},$$

$$\mathbf{S}_{12} = \mathbf{M}_{22}^{-1},$$

$$\mathbf{S}_{21} = \mathbf{M}_{11} - \mathbf{M}_{12} \cdot \mathbf{M}_{22}^{-1} \cdot \mathbf{M}_{21},$$

$$\mathbf{S}_{22} = \mathbf{M}_{12} \cdot \mathbf{M}_{22}^{-1}.$$

APPENDIX B: DETERMINATION OF THE COUPLING FACTOR

To illustrate the static coupling behavior, we plot in Fig. 10 the transmission coefficients without modulation for various values of coupling factor, α . Figure 10(a) displays the classical resonances of the single slab, while Figs. 10(b)–10(d) are the transmission curves for the case of two coupled static slabs for different values of α . As we increase the coupling factor, the scattering changes and average transmission bandwidth become smaller, while stronger undulations of the transmission coefficient appear. Strong coupling is desired to achieve strong nonreciprocity and frequency conversion.

APPENDIX C: PRESET VALUE OF THE INITIAL PHASE DIFFERENCE

To verify the consistency of the preset phase difference, $\Delta\phi = 0.5$, a series of calculations are performed upon $\Delta\phi$. Figure 11 presents the absolute value of difference between the right and left transmission coefficients of the fundamental mode, $||t_0^+ - |t_0^-||$, as a function of $\Delta\phi$ for the considered modulating frequencies, $F_m = 0.7, 0.9$, and 1.1 . For these three cases, a high level of transmission difference, indicating strong nonreciprocity, appears where $\Delta\phi$ is between 0.4π and 0.6π . To conclude, it is rational to assume strong asymmetry at $\Delta\phi = 0.5$.

APPENDIX D: SECOND-LEVEL FINE-TUNING

For $F_{in} = 8$ and $F_m = 0.76$, we perform a refinement of the optimization for stronger nonreciprocity. Figures 12(a) and 12(b) show $|T_0^+ - T_0^-|$ and $|10\log_{10}(T_0^+/T_0^-)|$, respectively, of the fundamental mode as a function of the static density ratio, δ , and phase difference, $\Delta\phi$, while Fig. 12(c) plots the total transmission difference. We can see that, with preselected $\delta = 5$ and $\Delta\phi = 0.5\pi$, the result is already good, so we just slightly change the value of $\Delta\phi$. The result of fine optimization is $\Delta\phi = 0.46\pi$ and $\delta = 5$, where $|T_0^+ - T_0^-| = 0.957$ and $|10\log_{10}(T_0^+/T_0^-)| = 27.15$ dB.

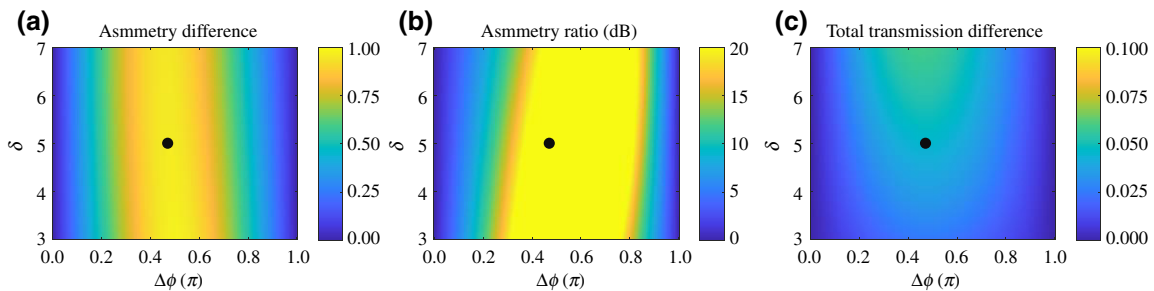


FIG. 12. Results of the theoretical calculation sweeping $\Delta\phi$ from zero to π and δ from three to seven, with $F_{in} = 8$ and $F_m = 0.76$ inherited from the last calculation. (a) Asymmetry difference of zeroth-order-mode transmittance. (b) Asymmetry ratio of zeroth-order-mode transmittance. (c) Total transmission difference. Black dots mark the point where $\Delta\phi = 0.46\pi$ and $\delta = 5$.

- [1] Romain Fleury, Dimitrios Sounas, Michael R. Haberman, and Andrea Alù, Nonreciprocal acoustics, *Acoust. Today* **11**, 14 (2015).
- [2] C. Rasmussen, L. Quan, and A. Alù, Acoustic nonreciprocity, *J. Appl. Phys.* **129**, 210903 (2021).
- [3] H. B. G. Casimir, On Onsager's principle of microscopic reversibility, *Rev. Mod. Phys.* **17**, 343 (1945).
- [4] J. W. Strutt, Some general theorems relating to vibrations, *Proc. London Math. Soc.* **s1-4**, 357 (1871).
- [5] B. Liang, B. Yuan, and J. Cheng, Acoustic Diode: Rectification of Acoustic Energy Flux in One-Dimensional Systems, *Phys. Rev. Lett.* **103**, 104301 (2009).
- [6] B. Liang, X. S. Guo, J. Tu, D. Zhang, and J. C. Cheng, An acoustic rectifier, *Nat. Mat.* **9**, 12 (2010).
- [7] X.-F. Li, X. Ni, L. Feng, M.-H. Lu, C. He, and Y.-F. Chen, Tunable Unidirectional Sound Propagation Through a Sonic-Crystal-Based Acoustic Diode, *Phys. Rev. Lett.* **106**, 084301 (2011).
- [8] X.-P. Wang, L.-L. Wan, T.-N. Chen, Q.-X. Liang, and A.-L. Song, Broadband acoustic diode by using two structured impedance-matched acoustic metasurfaces, *Appl. Phys. Lett.* **109**, 044102 (2016).
- [9] X. Wen, X. Zhu, A. Fan, W. Y. Tam, J. Zhu, F. Lemoult, M. Fink, and J. Li, Asymmetric frequency conversion with acoustic Non-hermitian space-time varying metamaterial, *J. Acoust. Soc. Am.* **146**, 863 (2019).
- [10] A. Oliner and A. Hessel, Guided waves on sinusoidally-modulated reactance surfaces, *IRE Trans. Antennas Propag.* **7**, 201 (1959).
- [11] E. S. Cassedy and A. A. Oliner, Dispersion relations in time-space periodic media: Part I—stable interactions, *Proc. IEEE* **51**, 1342 (1963).
- [12] E. S. Cassedy, Waves guided by a boundary with time—space periodic modulation, *Proc. Inst. Electr. Eng.* **112**, 269 (1965).
- [13] Y. Hadad, D. L. Sounas, and A. Alu, Space-time gradient metasurfaces, *Phys. Rev. B* **92**, 100304 (2015).
- [14] S. Taravati, Self-Biased broadband magnet-free linear isolator based on one-way space-time coherency, *Phys. Rev. B* **96**, 235150 (2017).
- [15] S. Taravati, N. Chamanara, and C. Caloz, Nonreciprocal electromagnetic scattering from a periodically space-time modulated slab and application to a quasisonic isolator, *Phys. Rev. B* **96**, 165144 (2017).
- [16] S. Taravati, Aperiodic space-time modulation for pure frequency mixing, *Phys. Rev. B* **97**, 115131 (2018).
- [17] S. Taravati, Giant Linear Nonreciprocity, Zero Reflection, And Zero Band Gap in Equilibrated Space-Time-Varying Media, *Phys. Rev. Appl.* **9**, 064012 (2018).
- [18] S. Taravati and G. V. Eleftheriades, Programmable nonreciprocal meta-prism, *Sci. Rep.* **11**, 1 (2021).
- [19] S. Taravati and G. V. Eleftheriades, Pure and Linear Frequency-Conversion Temporal Metasurface, *Phys. Rev. Appl.* **15**, 064011 (2021).
- [20] R. Fleury, D. L. Sounas, and A. Alù, Subwavelength ultrasonic circulator based on spatiotemporal modulation, *Phys. Rev. B* **91**, 174306 (2015).
- [21] C. Shen, X. Zhu, J. Li, and S. A. Cummer, Non-reciprocal acoustic transmission in space-time modulated coupled resonators, *Phys. Rev. B* **100**, 054302 (2019).
- [22] X. Zhu, J. Li, C. Shen, X. Peng, A. Song, L. Li, and S. A. Cummer, Non-Reciprocal acoustic transmission via space-time modulated membranes, *Appl. Phys. Lett.* **116**, 034101 (2020).
- [23] M. Oudich, Y. Deng, M. Tao, and Y. Jing, Space-time phononic crystals with anomalous topological edge states, *Phys. Rev. Res.* **1**, 033069 (2019).
- [24] G. Trainiti and M. Ruzzene, Non-reciprocal elastic wave propagation in spatiotemporal periodic structures, *New J. Phys.* **18**, 083047 (2016).
- [25] Y. Wang, B. Yousefzadeh, H. Chen, H. Nassar, G. Huang, and C. Daraio, Observation of Nonreciprocal Wave Propagation in a Dynamic Phononic Lattice, *Phys. Rev. Lett.* **121**, 194301 (2018).
- [26] G. Trainiti, Y. Xia, J. Marconi, G. Cazzulani, A. Erturk, and M. Ruzzene, Time-Periodic Stiffness Modulation in Elastic Metamaterials for Selective Wave Filtering: Theory and Experiment, *Phys. Rev. Lett.* **122**, 124301 (2019).
- [27] K. Yi, M. Ouisse, E. Sadoulet-Reboul, and G. Matten, Active metamaterials with broadband controllable stiffness for tunable band gaps and Non-reciprocal wave propagation, *Smart Mater. Struct.* **28**, 065025 (2019).
- [28] C. Sugino, M. Ruzzene, and A. Erturk, Nonreciprocal piezoelectric metamaterial framework and circuit strategies, *Phys. Rev. B* **102**, 014304 (2020).
- [29] M. Farhat, S. Guenneau, P.-Y. Chen, and Y. Wu, Spacetime modulation in floating thin elastic plates, *Phys. Rev. B* **104**, 014308 (2021).
- [30] R. Fleury, D. L. Sounas, C. F. Sieck, M. R. Haberman, and A. Alù, Sound isolation and giant linear nonreciprocity in a compact acoustic circulator, *Science* **343**, 516 (2014).
- [31] Z. Chen, C. Xue, L. Fan, S. Zhang, X. Li, H. Zhang, and J. Ding, A tunable acoustic metamaterial with double-negativity driven by electromagnets, *Sci. Rep.* **6**, 1 (2016).
- [32] C. Shen, J. Li, Z. Jia, Y. Xie, and S. A. Cummer, Non-reciprocal acoustic transmission in cascaded resonators via spatiotemporal modulation, *Phys. Rev. B* **99**, 134306 (2019).
- [33] M. Chegnizadeh, M. Memarian, and K. Mehrany, Non-reciprocity using quadrature-phase time-varying slab resonators, *J. Opt. Soc. Am. B* **37**, 88 (2020).
- [34] Q. Wang, Y. Yang, X. Ni, Y.-L. Xu, X.-C. Sun, Z.-G. Chen, L. Feng, X. Liu, M.-H. Lu, and Y.-F. Chen, Acoustic asymmetric transmission based on time-dependent dynamical scattering, *Sci. Rep.* **5**, 1 (2015).
- [35] G. J. Jeon and J. H. Oh, Nonlinear acoustic metamaterial for efficient frequency down-conversion, *Phys. Rev. E* **103**, 012212 (2021).
- [36] J. D. Schneider, T. Lu, S. Tiwari, X. Zou, A. Mal, R. N. Candler, Y. E. Wang, and G. P. Carman, Frequency conversion through nonlinear mixing in acoustic waves, *J. Appl. Phys.* **128**, 064105 (2020).
- [37] E. Riva, J. Marconi, G. Cazzulani, and F. Braghin, Generalized plane wave expansion method for non-reciprocal discretely modulated waveguides, *J. Sound Vib.* **449**, 172 (2019).
- [38] P. J. Westervelt, Parametric acoustic array, *J. Acoust. Soc. Am.* **35**, 535 (1963).
- [39] A. Moussatov, B. Castagnède, and V. Gusev, Frequency up-conversion and frequency down-conversion of acoustic waves in damaged materials, *Phys. Lett. A* **301**, 281 (2002).